Monthly Notices of the ROYAL ASTRONOMICAL SOCIETY

MNRAS **504,** 4460–4471 (2021) doi:10.1093/mnras/stab1185
Advance Access publication 2021 April 28

Nitrogen X-ray absorption in the local ISM

Efrain Gatuzz,[1]★ Javier A. García[2,3] and Timothy R. Kallman[4]

[1]*Max-Planck-Institut für extraterrestrische Physik, Gießenbachstraße 1, D-85748 Garching, Germany*
[2]*Cahill Center for Astronomy and Astrophysics, California Institute of Technology, Pasadena, CA 91125, USA*
[3]*Dr. Karl Remeis-Observatory and Erlangen Centre for Astroparticle Physics, Sternwartstr 7, D-96049 Bamberg, Germany*
[4]*NASA Goddard Space Flight Center, Greenbelt, MD 20771, USA*

Accepted 2021 April 21. Received 2021 April 21; in original form 2020 September 17

ABSTRACT

Nitrogen is one of the most abundant metals in the interstellar medium (ISM), and thus it constitutes an excellent test to study a variety of astrophysical environments, ranging from nova to active galactic nuclei. We present a detailed analysis of the gaseous component of the N K-edge using high-resolution *XMM–Newton* spectra of 12 Galactic and 40 extragalactic sources. For each source, we have estimated column densities for N I, N II, N III, N V, N VI, and N VII ionic species, which trace the cold, warm, and hot phases of the local Galactic ISM. We have found that the cold-warm component column densities decrease with the Galactic latitude, while the hot component does not. Moreover, the cold column density distribution is in good agreement with UV measurements. This is the first detailed analysis of the nitrogen K-edge absorption due to ISM using high-resolution X-ray spectra.

Key words: ISM: abundances – ISM: atoms – ISM: structure – Galaxy: structure – X-rays: ISM.

1 INTRODUCTION

The interstellar medium (ISM), defined as gas and dust between stars, is a key ingredient in the Galactic dynamics. The ISM shows multiple phases, characterized by different gas temperatures which vary from 10 to 10^6 K (e.g. McKee & Ostriker 1977; Falgarone et al. 2005; Draine 2011; Jenkins & Tripp 2011; Stanimirović & Zweibel 2018). In this sense, high-resolution X-ray spectroscopy is a powerful technique to study such environment because, due to their high energy, X-ray photons interact with the cold (including molecules and dust), warm, and hot components (Juett, Schulz & Chakrabarty 2004; Juett et al. 2006; Pinto et al. 2010; Liao, Zhang & Yao 2013; Pinto et al. 2013; Luo & Fang 2014; Nicastro et al. 2016a; Gupta, Mathur & Krongold 2017; Gatuzz & Churazov 2018; Gatuzz et al. 2018b).

Among the most abundant metals in the ISM, nitrogen constitutes an excellent diagnostic tool to study a variety of astrophysical environments. For example, Ness et al. (2003) identified H- and He-like N absorption lines by a white dwarf outflow following the outburst of nova V4743 Sagittarii. Steenbrugge et al. (2005a) identified an N VI Lyα absorption line associated with a warm absorber in the *XMM–Newton* X-ray spectra of the Seyfert 1 galaxy IC 4329A. Steenbrugge et al. (2005b) identified an N V Kα absorption line as 29.42 Å in the outflow of the Seyfert 1 galaxy NGC 5548. Smith, Page & Branduardi-Raymont (2007) performed a detailed analysis of the soft X-ray spectrum of the Seyfert 1 galaxy Mrk 509 using *XMM–Newton* observations. They found three warm absorber phases traced, among others, by N VI and N VII absorption lines. Ramírez et al. (2008) identified N VI Kα and N VI Kβ absorption lines in the warm absorber of the MR 2251−178 quasar, tracing an outflow of ionized material. Ness et al. (2011) analysed *XMM–Newton* observations of the fast classical nova V2491 Cyg. They found absorption lines due to N I associated with the ISM and photospheric lines ionic species such as N VI and N VII, tracing the dynamics of the ejecta.

In order to model the complexity of the photoabsorption K-edge, located at the 24–32 Å wavelength band, the accuracy of atomic data is crucial, to avoid misidentification and misinterpretation of the observed absorption features. In the last few years we have performed benchmarking of the atomic data by comparing theoretical calculations, astronomical observations, and laboratory measurements for species found in the ISM such as carbon (Gatuzz et al. 2018a), oxygen (García et al. 2005; Gorczyca et al. 2013; Gatuzz et al. 2013a, b), neon (Gatuzz et al. 2015), magnesium (Hasoğlu et al. 2014), and silicon (Gatuzz et al. 2020). Following such studies, we present an analysis of the N K-edge absorption region using *XMM–Newton* observations of low-mass X-ray binaries (LMXBs) and extragalactic sources. We describe the data sample and the spectral fitting procedure in Section 2. Section 3 shows a discussion of the results obtained from the fits. Finally, Section 4 summarizes the main results of our analysis.

2 X-RAY OBSERVATIONS AND SPECTRAL FITTING

We have compiled a data sample of 12 LMXBs and 40 extragalactic sources from the *XMM–Newton* Science Archive (XSA). We selected observations with more than 1000 counts in the 24–32 Å band (i.e. the N photoionization K-edge absorption region). In order to get an unbiased sample, we did not impose any constraints in the

★ E-mail: efraingatuzz@gmail.com

© 2021 The Author(s)
Published by Oxford University Press on behalf of Royal Astronomical Society

Downloaded from https://academic.oup.com/mnras/article/504/3/4460/6256854 by NASA Goddard Space Flight Ctr user on 11 January 2022

Table 1. List of Galactic observations analysed.

Source	Galactic coordinates	Distance (kpc)	N(H I)	Exposure time (ks)	Number counts (24–32 Å)
4U 1254–69	(303.4, −6.4)	13.0 ± 3.0^{a}	3.46	233	66 936
4U 1543–62	(321.76, −6.34)	7.0^{b}	3.79	50	35 103
4U 1636–53	(332.9, −4.8)	6.0 ± 0.5^{c}	4.04	379	137 151
4U 1735–44	(346.0, −6.9)	9.4 ± 1.4^{d}	3.96	107	85 494
4U 1820−30	(2.7, −7.9)	7.6 ± 0.4^{e}	1.33	81	381 038
4U 1957+11	(51.31, −9.33)	$20 < d < 40^{f}$	1.98	85	65 478
Aql X–1	(37.7, −4.1)	5.2 ± 0.8^{d}	4.30	165	43 229
Cygnus X-2	(87.3, −11.3)	13.4 ± 2^{d}	1.90	342	633 707
GS 1826–238	(9.3, −6.1)	6.7^{c}	3.00	347	87 798
GX 9 + 9	(8.5,9.0)	4.4^{g}	3.31	80	108 956
HETEJ1900.1−2455	(11.30, −12.87)	5^{h}	1.76	71	57 691
SAXJ1808.4−3658	(355.39, −8.15)	2.8^{c}	1.76	173	568 390
Serpens X–1	(36.12,4.84)	11.1 ± 1.6^{d}	5.42	66	20 858
Swift J1753.5–0127	(24.89,12.18)	$8.42^{+4.32}_{-2.85}$ ^{i}	2.98	249	428 804

Notes. N(H I) in units of 10^{21} cm^{-2}.
Distances obtained from [a]in't Zand et al. (2003); [b]Wang & Chakrabarty (2004);
[c]Galloway et al. (2008); [d]Jonker & Nelemans (2004); [e]Kuulkers et al. (2003);
[f]Gomez, Mason & Robinson (2015); [g]Grimm, Gilfanov & Sunyaev (2002); [h]Hynes et al. (2004); [i]Gandhi et al. (2019).

significance of the detection for a particular line (e.g. N VI Kα detection). Tables 1 and 2 list the analysed Galactic and extragalactic sources, respectively, including the Galactic coordinates, H I column densities, which are taken from Willingale et al. (2013), total exposure times, and total number of counts of all observations in the N K-edge. The distances to the sources are included for all LMXBs. Observations were reduced using the Science Analysis System (SAS,[1] version 18.0.0) including background subtraction and following the standard procedure to obtain high-resolution spectra from the Reflection Grating Spectrometers (RGS, den Herder et al. 2001). In particular, we follow the SAS thread to reduce RGS data and extract spectra of point-like sources. Using the `rgsproc` task, the procedure included the filtering of events and exposure, to exclude flaring background, and the creation of response matrices. Each spectrum was rebinned to have at least 1 count per channel.

For each source, all observations were fitted simultaneously using the XSPEC package (version 12.10.1[2]) in the 24–32 Å wavelength region. The continuum was modelled with a `powerlaw*constant` model, where the Photon-Index was set free to vary but tied among all the observations of the same source, while the `constant` accounts for differences in the normalization among them. Moreover, we used `cash` statistics (Cash 1979) in the spectral fitting analysis.

2.1 Nitrogen photoabsorption cross-sections

We use the K-edge photoionization cross-sections for N II–N V computed by García et al. (2009), which include detailed calculations of atomic properties of K-vacancy states for all ions of the nitrogen isonuclear sequence. Importantly, the smearing of the K-edge due to both Auger and radiation damping is taken into account. In the cases of N VI and N VII, we used the K-edge photoionization cross-sections from the Opacity Project (Badnell et al. 2005). Fig. 1 shows the photoabsorption cross-sections included in the model, which includes the cold, warm, and hot phases of the ISM.

[1]https://www.cosmos.esa.int/web/xmm-newton/sas
[2]https://heasarc.gsfc.nasa.gov/xanadu/xspec/

We included these N photoabsorption cross-sections in a modified version of the `ISMabs` model (Gatuzz et al. 2015), thus allowing the column densities for the ionic species of interest to be free parameters in the data fitting. We fixed the H I `ISMabs` column densities to the values provided by Willingale et al. (2013). For each source, the column densities were linked between the different observations. We note that a detailed benchmarking of the main doublet/triplet resonance line positions (see Fig. 1) cannot be performed given that the differences in their relative positions are smaller than the instrumental spectral resolution. For example, for N II Kα and N III Kα we have a minimum separation for contiguous peaks of $\Delta\lambda \sim 22.1$ mÅ and $\Delta\lambda \sim 31.2$ mÅ, respectively, while the RGS resolution in the N K-edge region is $\Delta\lambda \sim 60$ mÅ. Therefore, we used the atomic data as computed by García et al. (2009), which estimated the accuracy of the K-threshold to be within 1 eV.

3 RESULTS FROM SPECTRAL FITS

The best-fitting results are listed in Table 3. We have found acceptable fits, from the statistical point of view, although for most of the sources we have obtained upper limits for the relevant parameters. We labelled the multiple phases of the gaseous ISM as cold (N I), warm (N II + N III), and hot (N V + N VI + N VII). Fig. 2 shows the best-fitting column densities obtained. We note that for the cold component the column densities are systematically larger for the Galactic sources (black points) than for the extragalactic sources (red points). For the warm-hot components, on the other hand, the column densities tend to be similar between both types of sources. Fig. 3 shows the distribution of the cold, warm, and hot column densities as a function of the Galactic latitude. The plot shows that the cold-warm column densities decrease with the Galactic latitude, while the hot component does not appear to show any correlation, although for this case most of the results correspond to upper limits. This implies that the cold component is mostly concentrated in the Galactic disc, while the hot component is more homogeneously distributed. Previous studies suggest that a single disc model cannot fit the hot component of the ISM but requires a spherically symmetric

Downloaded from https://academic.oup.com/mnras/article/504/3/4460/6256854 by NASA Goddard Space Flight Ctr user on 11 January 2022

Table 2. List of extragalactic observations analysed.

Source	Galactic coordinates	N(H I)	Exposure time (ks)	Number of counts (24–32 Å)
1ES 1028+511	(161.44; 54.44)	1.26	300	61 972
1ES 1553+113	(21.91; 43.96)	4.35	2065	396 199
1H 0414+009	(191.81; −33.16)	13.70	91	12 194
1H 0707–495	(260.17; −17.67)	6.55	1395	127 334
1H 1219+301	(186.36; 82.73)	0.20	29	29 318
1H 1426+428	(77.49; 64.90)	1.14	425	145 627
3C 120	(190.37; −27.40)	19.30	305	19 907
3C 273	(289.95; 64.36)	1.78	1426	912 126
3C 279	(305.10; 57.06)	2.22	153	10 181
3C 390.3	(111.44; 27.07)	4.51	123	29 626
Ark 120	(201.69; −21.13)	1.40	773	203 191
Ark 564	(92.14; −25.34)	6.74	890	556839
ESO 141–G055	(338.18; −26.71)	6.41	268	69 813
ESO 198–G24	(271.64; −57.95)	3.27	178	20 460
Fairall 9	(295.07; −57.83)	3.43	328	42 360
H2356–309	(12.84; −78.04)	1.48	702	91 678
H1821+643	(94.00; 27.42)	0.39	121	22 990
HE1143−1810	(281.85; 41.71)	0.34	184	51 334
IRAS13349+2438	(20.60; 79.32)	1.07	199	24 152
IC4329A	(317.50; 30.92)	0.56	165	19 327
IZw1	(123.75; −50.17)	6.01	382	50 616
MCG-6-30-15	(313.29; 27.68)	0.47	794	341 504
MR2251–178	(46.20; −61.33)	2.67	592	131 180
Mrk 279	(115.04; 46.86)	1.72	188	74 129
Mrk 421	(179.83; 65.03)	2.01	3004	7.37×10^6
Mrk 501	(63.60; 38.86)	1.66	200	109 344
Mrk 509	(35.97; −29.86)	5.04	835	498 007
Mrk 766	(190.68; 82.27)	0.19	739	223 087
Mrk 841	(11.21; 54.63)	2.43	206	35 132
NGC 3783	(287.46; 22.95)	13.80	486	46 906
NGC 4593	(297.48; 57.40)	2.04	386	97 579
NGC 5548	(31.96; 70.50)	1.69	1025	108 103
NGC 7213	(349.59; −52.58)	1.12	181	22 796
NGC 7469	(83.10; −45.47)	5.24	857	229 214
PG1116+215	(223.36; 68.21)	1.43	393	49 771
PKS 0548–32	(237.57; −26.14)	2.87	254	58 464
PKS 0558–504	(257.96; −28.57)	4.18	933	420 921
PKS 2005–489	(350.37; −32.60)	4.66	253	22 609
PKS 2155–304	(17.73; −52.25)	1.63	2000	2.53×10^6
Tons 180	(138.99; −85.07)	1.54	222	42 199

Note. N(H I) in units of 10^{20} cm^{-2}

profile, to account for the Galactic halo contribution (Miller & Bregman 2013, 2015; Nicastro et al. 2016b; Gatuzz & Churazov 2018).

The presence of absorption features due to material intrinsic to the source (e.g. warm absorbers in active galactic nuclei) may lead to misidentification of certain absorption lines. To study such intrinsic absorber we used the `warmabs` model, which is computed with the XSTAR photoionization code (Kallman & Bautista 2001). This model considers the physical conditions for an ionizing source surrounded by a gas and takes into account physical processes such as photoionization, dielectronic and radiative recombination, excitation and electron impact collisional ionization. The model assumes ionization equilibrium conditions, a Maxwellian electron velocity distribution, and that the gas responsible for emission and absorption has a uniform temperature and ionization throughout. The parameters of the model includes the column density of the absorber (NHI), the ionization parameter ($\log \xi$), elemental abundances (Ax), broadening turbulence ($v_{\rm turb}$), and redshift (z).

We have tested the effects in the `ISMabs` column densities when including a `warmabs` component in addition to the `ISMabs` components, for Ark 564. In order to account for variations in the spectral energy distribution (SED), which affects the photoionization rate, we fitted the `warmabs` N(H I) and $\log \xi$ parameters independently for each observation, while the `ISMabs` column densities were linked between the different observations (i.e. to account for the ISM contribution). We have found that the `warmabs` best fit prefers a highly ionized component, but the `warmabs` column densities for such component are poorly constrained. Moreover, while the cold and warm `ISMabs` column densities obtained are not affected by the inclusion of `warmabs`, the uncertainties in `ISMabs` column densities for the hot component increase significantly. Similar results were obtained for other sources with large number

Downloaded from https://academic.oup.com/mnras/article/504/3/4460/6256854 by NASA Goddard Space Flight Ctr user on 11 January 2022

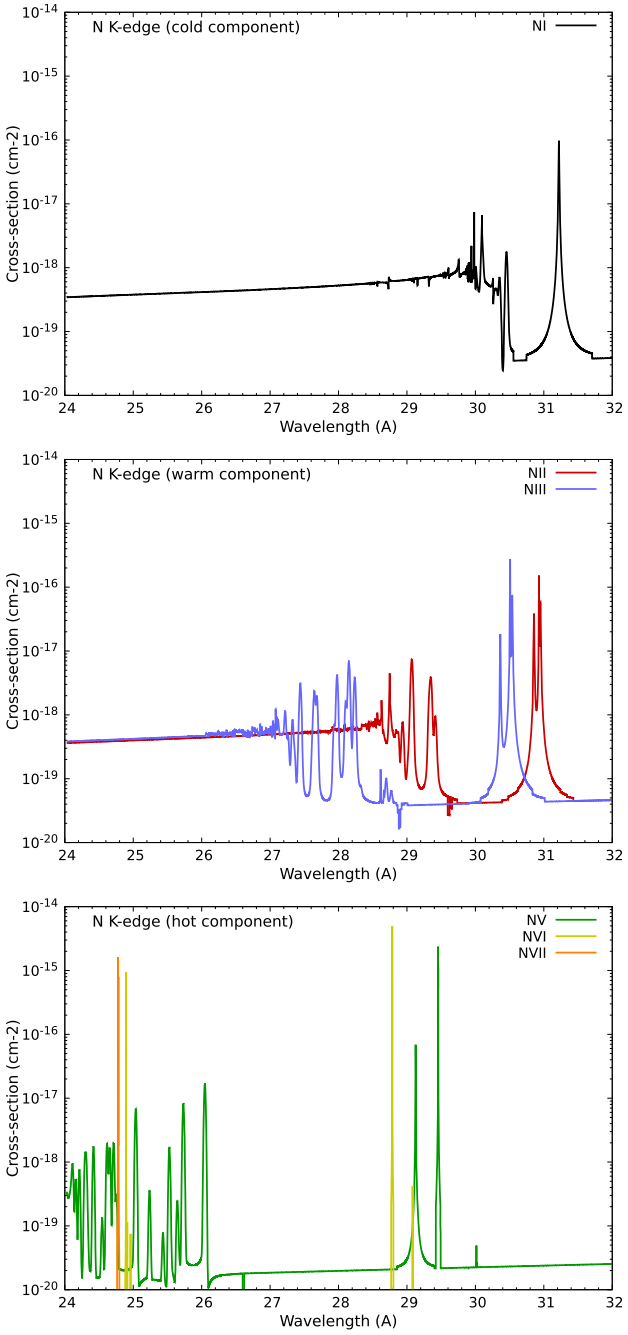


Figure 1. N I (top panel), N II, N III (middle panel), N V, N VI, and N VII (bottom panel) photoabsorption cross-sections computed by García et al. (2009) and included in the model.

of counts, including 1ES1028+511, 1ES1553+113, 1H0414+009, and 1H0707−495. It is important to note that the fits here presented are done within a small wavelength region (24–32 Å). In order to perform a more detailed analysis of the absorber associated with the sources, a complete analysis of the RGS data is desired to identified absorption features in the spectra due to different ions, apart from nitrogen. However, such analysis is beyond the scope of this work. Finally, it is important to note that when fitting independently the intrinsic absorber for different observations, the computation time to perform error calculation increases exponentially (e.g. there are 37 observations for Mrk 421).

3.1 Comparison with previous works

We have collected N I column density values from previous studies. Meyer, Cardelli & Sofia (1997, MEY + 97) analysed the interstellar N I λλ 1160,1161 absorption doublet towards eight stars using the *Hubble Space Telescope* Goddard High Resolution Spectrograph (GHRS). Moos et al. (2002, MOO + 02) determined N I column densities along seven lines of sight using N I λ 1160 observations obtained with the Far Ultraviolet Spectroscopic Explorer (FUSE). Knauth, Meyer & Lauroesch (2006, KNA + 06) reported on the analysis of 13 stars using FUSE observations. Finally, Gudennavar et al. (2012, GUD + 12) created a data base of multiple interstellar column densities using absorption line data towards 3008 stars, 164 of them with N I values.

Fig. 4 shows the distribution of N I values as a function of Galactic latitude (top panel) and distance (bottom panel) including the collected sample. In the case of the distances, we have not included the LMXB 4U1957+11 due to its large uncertainty. For the cold ISM component, it is expected to show a strong correlation between the column densities and the Galactic latitude (see for example Gatuzz & Churazov 2018). For the cold component of the ISM, it is commonly assumed in the literature to be exponentially decreasing perpendicular to the Galactic plane, with larger column densities near the Galactic centre (see e.g. Robin et al. 2003; Kalberla & Kerp 2009). For the X-ray data we have included only those Galactic sources for which N I is well constrained (i.e. no upper limits. See Table 3). We found that the X-ray column densities derived from the spectral fitting are in good agreement with previous results, with a clear tendency to decrease as we move away from the Galactic plane ($|Latitude| > 50^\circ$) with variations in regions that form stars more actively than others (e.g. spiral arm regions such as Vela or Orion). However, the number of lines of sight does not allow to cover small-scale structure (i.e. au) but rather large-scale. Finally, it is important to note that the hot component is only accessible through UV/X-ray observations.

3.2 ISM structure

Previous analysis of the ISM multiphase structure using X-ray absorption technique has shown that the gas physical state is dominated by the cold component, with mass fractions for the ISM phases in the Galactic disc of cold $\sim$ 90 per cent, warm $\sim$ 8 per cent, and hot $\sim$ 2 per cent components (e.g. Yao & Wang 2006; Piontek & Ostriker 2007; Pinto et al. 2013; Gatuzz & Churazov 2018). The uncertainties in the `ISMabs` column densities obtained prevent us to compute accurate mass fractions for all sources. For example, we noted that our best-fitting results show a very large contribution of the N VII column density associated with the hot component (e.g. GX9+9, 3C 273, MCG–6-30-15, Mrk766, PKS2005−489), while previous work indicates that the hot phase represent less than 1 per cent of the total ISM (e.g. Pinto et al. 2013). However, for these sources our analysis show that the rest of ionic species are not well constrained. Moreover, our `ISMabs` model includes the column densities as free parameters in the model and therefore we do not consider any ionization balance for the nitrogen ionic species. In this sense, a proper definition requires a spectral fitting with a more complete physical model that compute ionization balance depending on temperature. The contribution of the different ISM phases depends on the location of the absorber. While the density distribution for the cold-warm components is typically modelled with an exponential profile for the Galactic disc, the hot component includes the contribution of the Galactic halo

Downloaded from https://academic.oup.com/mnras/article/504/3/4460/6256854 by NASA Goddard Space Flight Ctr user on 11 January 2022

Table 3. Best-fitting nitrogen column densities obtained.

Source	N I	N II	N III	N V	N VI	N VII	cash/d.o.f.
			Galactic sources				
4U 1254–690	<12.2	<3.8	<0.7	<0.4	<40.9	<22.3	4355/3974
4U 1543–62	<5.9	<1.7	<0.0	<1.7	<16.0	<19.9	859/790
4U 1636–53	$31.2^{+12.7}_{-10.8}$	$3.9^{+5.6}_{-3.0}$	<2.1	<0.2	<29.5	<10.5	9010/7969
4U 1735–44	$20.7^{+7.7}_{-7.6}$	<1.3	<0.6	<0.4	<56.7	<17.9	1684/1587
4U 1957+11	<2.8	<1.1	<0.2	<1.3	<31.5	<0.5	1693/1587
4U 1820−30	4.3 ± 2.2	$0.87^{+0.56}_{-0.46}$	$0.67^{+0.48}_{-0.36}$	<0.2	<0.1	<0.02	2367/1587
Aql X–1	$81.2^{+22.0}_{-25.5}$	$3.9^{+5.6}_{-2.9}$	2.1 ± 1.3	<2.1	<17.4	<0.7	2694/2383
Cygnus X–2	11.3 ± 2.4	$0.58^{+0.40}_{-0.34}$	<0.3	<0.8	<0.5	<0.1	3971/2382
GS1826–238	$48.4^{+11.8}_{-13.7}$	$4.1^{+3.9}_{-2.8}$	<1.6	<1.1	<10	<0.3	4577/3986
GX9+9	$15.2^{+7.8}_{-7.6}$	<1.8	<0.6	<1.5	<14.2	$121.0^{+46.3}_{-46.1}$	1711/1588
HETEJ1900.1–2455	$7.5^{+5.0}_{-4.5}$	<0.8	$0.8^{+1.1}_{-0.7}$	<1.6	<29.6	<27.7	849/790
SAXJ1808.4–3658	$3.1^{+1.2}_{-1.1}$	$2.8^{+0.6}_{-0.5}$	$0.26^{+0.19}_{-0.16}$	<0.1	<3.9	<6.4	2334/1589
Serpens X–1	$9.1^{+8.9}_{-5.6}$	<4.7	<4.1	<2.4	<1.2	<0.9	2555/2384
Swift J1753.5–0127	$14.0^{+3.7}_{-2.4}$	1.1 ± 0.6	$0.28^{+0.28}_{-0.23}$	<0.2	<2.1	<10.3	8031/5556
			Extragalactic sources				
1ES1028+511	<2.9	<0.9	<0.5	<1.2	<39.0	<6.1	2373/2381
1ES1553+113	$0.9^{+0.9}_{-0.7}$	<0.3	<0.2	$0.8^{+0.6}_{-0.6}$	<4.2	<9.9	18237/17547
1H0414+009	<9.2	<1.9	<4.0	<4.5	<45.3	<23.6	1681/1586
1H0707−495	<2.5	$2.0^{+1.4}_{-1.1}$	<0.5	<3.1	<26.3	<38.5	8939/8763
1H1219+301	<1.1	<0.8	<2.6	<0.2	<7.1	<19.5	790/789
1H1426+428	<1.2	<0.5	$0.32^{+0.43}_{-0.30}$	<0.4	<17.2	<3.2	4727/4770
3C 120	<4.3	$5.8^{+6.3}_{-4.2}$	<1.6	<0.1	<39.4	<1.9	828/788
3C 273	<0.4	0.21 ± 0.14	0.31 ± 0.12	<0.4	$30.6^{+8.2}_{-7.9}$	$22.9^{+15.5}_{-13.2}$	33390/29457
3C 279	<3.7	<3.7	<5.7	<1.1	<57.8	<0.1	870/791
3C 390.3	<1.5	<2.3	$1.4^{+2.3}_{-1.3}$	<4.1	$76.9^{+55.8}_{-53.9}$	<48.8	1555/1585
Ark120	$2.1^{+2.1}_{-1.4}$	<0.5	<0.3	<0.8	<17.5	<13.9	5036/4779
Ark564	$2.14^{+0.98}_{-0.81}$	$0.51^{+0.24}_{-0.22}$	$0.26^{+0.16}_{-0.14}$	0.9 ± 0.4	<1.1	<9.4	12412/10357
ESO141−G055	$1.72^{+2.63}_{-1.58}$	<0.7	<1.2	<0.7	$38.7^{+30.2}_{-27.6}$	<55.7	3467/3183
ESO198−G24	<8.4	<1.7	<2.2	<5.5	<55.4	<43.8	1575/1584
Fairall9	<2.3	<0.4	<0.7	<0.8	$38.2^{+38.6}_{-34.8}$	<33.2	2522/2385
H1426+428	<1.6	<0.5	<0.7	<0.4	$18.5^{+18.8}_{-15.4}$	<10.7	5078/4771
H1821+643	<5.9	<2.1	<3.0	<3.3	<16.3	<8.2	7958/7174
H2356−309	<2.7	<0.3	<0.2	<1.3	<22.9	<29.2	6799/6373
HE1143−1810	$2.2^{+3.4}_{-1.9}$	$1.1^{+1.2}_{-0.9}$	<0.3	<1.5	$47.5^{+35.1}_{-33.0}$	<60.8	4983/4779
IZw1	<2.4	<0.9	$0.88^{+1.33}_{-0.76}$	<1.5	<3.0	<30.8	3595/3181
MCG-6-30-15	$1.8^{+0.9}_{-0.8}$	$0.45^{+0.36}_{-0.31}$	$0.36^{+0.27}_{-0.22}$	$2.3^{+0.9}_{-1.2}$	$1.5^{+2.9}_{-1.2}$	$50.6^{+19.4}_{-15.6}$	9528/7165
MR2251−178	<0.5	<0.5	$0.53^{+0.57}_{-0.38}$	<0.2	<3.4	13.7	7112/6375
Mrk279	<1.8	<0.8	<0.7	<1.7	<30.3	<51.0	3290/3178
Mrk421	0.41 ± 0.11	0.36 ± 0.05	0.20 ± 0.03	<0.02	$2.2^{+1.6}_{-1.5}$	$1.4^{+1.2}_{-0.8}$	60741/29471
Mrk501	<0.5	<0.3	<0.4	<1.3	<24.2	<0.2	5044/4777
Mrk509	$1.01^{+0.97}_{-0.67}$	$0.34^{+0.23}_{-0.21}$	<0.13	$0.40^{+0.36}_{-0.24}$	$14.1^{+8.5}_{-7.5}$	<7.0	12739/10361
Mrk766	<0.9	<0.4	<0.3	<2.3	$3.11^{+7.87}_{-3.05}$	$38.8^{+36.6}_{-35.6}$	7194/6359
Mrk841	<5.6	<1.4	<0.4	<1.6	$83.7^{+48.0}_{-47.3}$	<59.5	5003/4773
NGC 3783	<7.1	<0.5	$3.5^{+2.8}_{-1.9}$	<2.5	<37.3	<38.9	3049/2382
NGC 4593	<1.2	<0.6	$0.74^{+0.70}_{-0.48}$	<0.7	$34.9^{+24.1}_{-23.2}$	<17.2	5333/4778
NGC 5548	<3.4	$1.8^{+1.6}_{-1.1}$	<0.3	<0.8	<29.2	<0.5	2806/2381
NGC 7213	<4.9	<1.5	$1.42^{+2.60}_{-1.27}$	<2.1	<72.9	<16.5	1762/1587
NGC 7469	<0.9	$1.3^{+0.6}_{-0.5}$	<0.3	<0.2	$31.2^{+15.1}_{-14.3}$	<14.4	9105/7967
PG1116+215	$3.3^{+5.3}_{-3.0}$	<1.8	<1.6	<0.3	<48.5	<96.2	3411/3182
PKS0548−32	<3.7	<1.4	<0.8	<1.2	<29.9	<13.0	2536/2381
PKS0558−504	<0.9	$0.39^{+0.35}_{-0.30}$	$0.39^{+0.30}_{-0.24}$	<0.3	<10.1	$17.7^{+22.6}_{-15.1}$	13007/11945
PKS2005−489	<2.5	$2.17^{+2.50}_{-1.56}$	<1.1	<0.8	<49.7	$53.3^{+79.2}_{-49.3}$	2608/2382
PKS2155−304	<0.1	<0.1	<0.3	<0.1	<11.8	<0.1	39762/27898
Tons180	<2.1	<0.5	<0.4	<1.1	<39.2	<82.3	3308/3181

Note. Column densities in units of 10^{16} cm^{-2}.

Downloaded from https://academic.oup.com/mnras/article/504/3/4460/6256854 by NASA Goddard Space Flight Ctr user on 11 January 2022

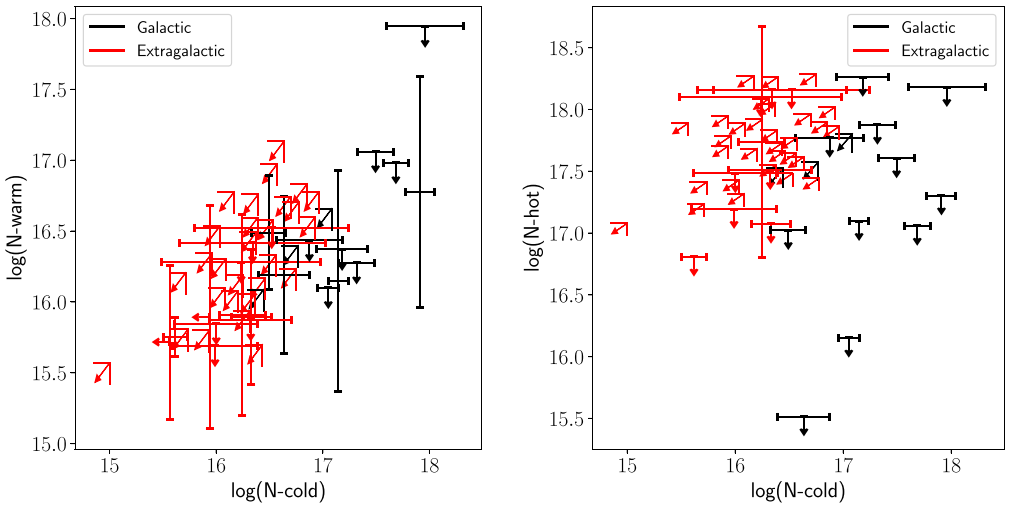


Figure 2. Best-fitting column densities for the cold (N I), warm (N II + N III), and hot (N V + N VI + N VII) ISM phases. The black data points correspond to LMXB, while the red points correspond to extragalactic sources.

(e.g. Miller & Bregman 2013, 2015; Nicastro et al. 2016b; Gatuzz & Churazov 2018). However, the absence of sources in our sample near the Galactic centre, a region heavily affected by the cold gas absorption, does not allow us to constrain the density profiles of the different ISM phases. More information about the physical properties of the gas (e.g. temperature and abundances) will be included in future works, with the inclusion of more complex models (e.g. `warmabs`).

3.3 Future prospects

Future X-ray high-resolution spectra mission, such as *Arcus* (Smith et al. 2016) and *Athena* (Nandra et al. 2013), will benefit greatly from this atomic data benchmarking. For example, Fig. 5 shows a 10 ks simulation for an extragalactic source (i.e. Mrk 421 in high-state) obtained with *Athena* for the baseline configuration.[3] The position for the main absorption lines are indicated. The plot shows the outstanding capabilities of the instrument, with the main resonance absorption lines visible by-eye, compared with the RGS spectra analysed in this paper. For such observation the line profiles can be studied with an accuracy at the per cent level. More important, by measuring simultaneously multiple resonance lines (e.g. Kα and Kβ) for the same ions, model-independent constraint on the broadening will be obtained.

4 CONCLUSIONS

We have carried out analysis of the ISM nitrogen K-edge absorption (24–32 Å) using high-resolution *XMM–Newton* spectra. Our data sample consist of 12 LMXBs and 40 extragalactic sources. For each source we fitted all observations simultaneously using a `powerlaw*constant` model for the continuum and a modified version of the `ISMabs` model for the spectral absorption features. We have found acceptable fits, from the statistical point of view, for most of sources. We have measured column densities for N I, N II, N III, N V, N VI, and N VII ionic species, which trace the cold, warm, and hot phases of the ISM. For the cold component we have found that the distribution of the column density distribution as a function of Galactic latitude is in good agreement with UV measurements. For the hot component we have not found such correlation, most likely due to the contribution from the Galactic halo. We have tested the effects in the `ISMabs` column densities when including a `warmabs` component, to account for absorption intrinsic to the sources. For such test, we link the ISM column densities between different observations (to account for the ISM contribution), while the `warmabs` N(H I) and $\log\xi$ parameters were fitted independently for each observation. We have found that both cold and warm `ISMabs` column densities obtained are not affected by the inclusion of the `warmabs` component. However, the uncertainties in the hot ISM phase increase significantly, while the column densities for the `warmabs` are not constrained. Such analysis point out the importance of modelling simultaneously multiple K-edge absorption regions (e.g. O, Ne, Mg) in order to study the contribution from both, the local ISM and intrinsic absorption. Future observations with new-generation instrumentation such as *Arcus* and *Athena* will allow a finer examination of the N K-edge structure.

[3] http://x-ifu-resources.irap.omp.eu/public/responses/cc_configuration/

ACKNOWLEDGEMENTS

We thank the anonymous referee for the careful reading of our manuscript and the valuable comments. JAG acknowledges support from the Smithsonian Astrophysical Observatory grant AR0-21003X, and from the Alexander von Humboldt Foundation.

DATA AVAILABILITY

Observations analysed in this article are available in the *XMM–Newton* Science Archive (XSA) (http://nxsa.esac.esa.int/nxsa-web/#search). The `ISMabs` model is included in the XSPEC data analysis software (https://heasarc.gsfc.nasa.gov/xanadu/xspec/).

Downloaded from https://academic.oup.com/mnras/article/504/3/4460/6256854 by NASA Goddard Space Flight Ctr user on 11 January 2022

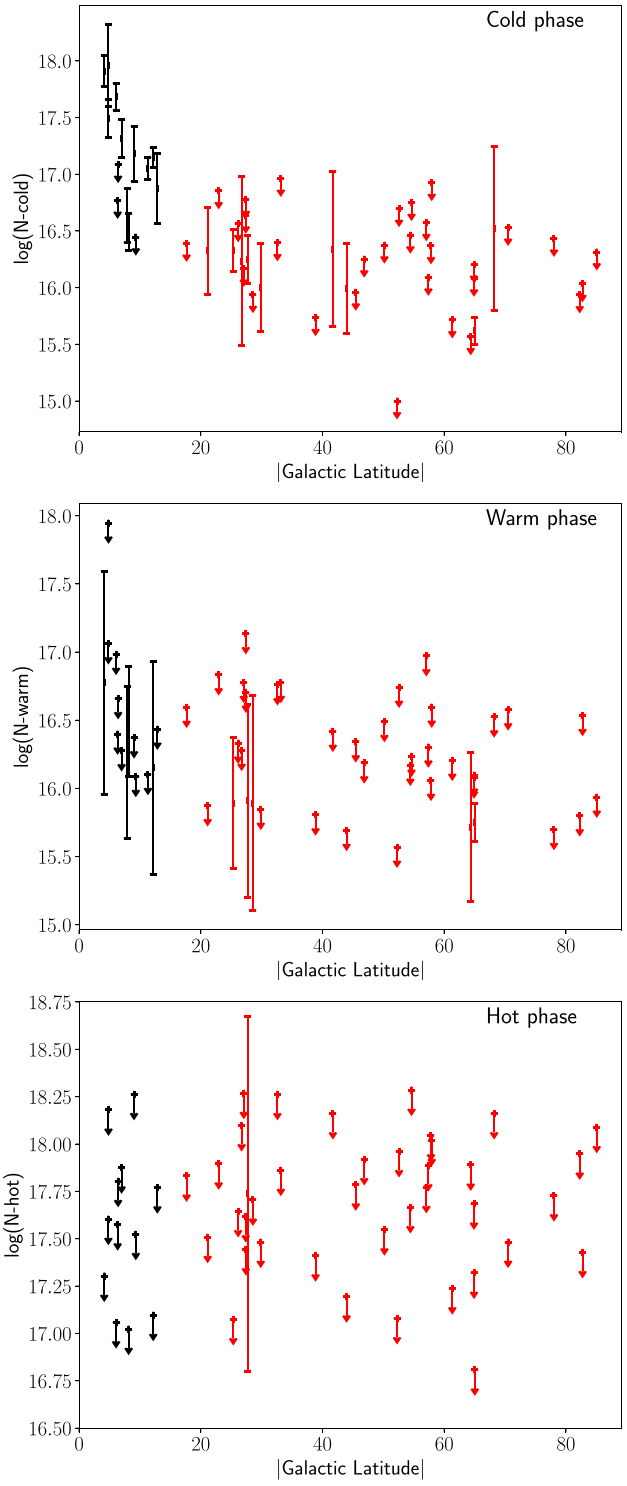


Figure 3. Best-fitting column densities for the cold (N I), warm (N II + N III), and hot (N V + N VI + N VII) ISM phases as a function of the Galactic latitude. The black data points correspond to LMXB, while the red points correspond to extragalactic sources.

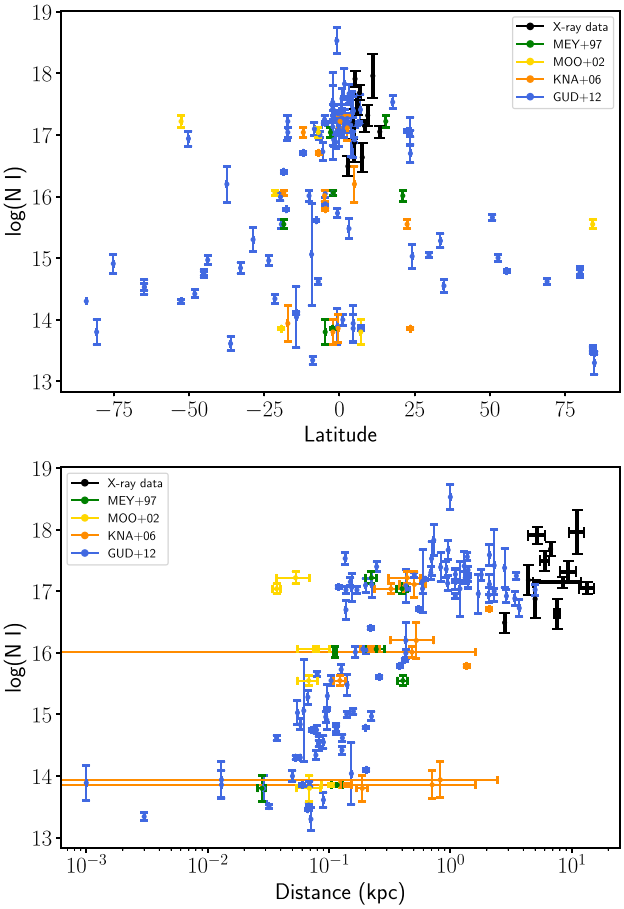


Figure 4. Top panel: N I column densities distribution as a function of Galactic latitude for different Galactic samples. Bottom panel: N I column densities distribution as a function of the distance.

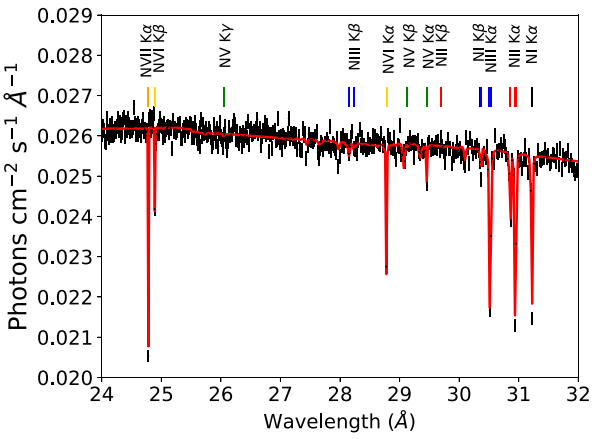


Figure 5. *Athena* simulation of the N K-edge photoabsorption region for an extragalactic source (e.g. Mrk 421). The total exposure time is 10 ks and the flux is $\log F_x = -9.77$ erg cm^{-2} s^{-1} in the 24–32 Å wavelength range.

Downloaded from https://academic.oup.com/mnras/article/504/3/4460/6256854 by NASA Goddard Space Flight Ctr user on 11 January 2022

REFERENCES

Badnell N. R., Bautista M. A., Butler K., Delahaye F., Mendoza C., Palmeri P., Zeippen C. J., Seaton M. J., 2005, MNRAS, 360, 458
Cash W., 1979, ApJ, 228, 939
den Herder J. W. et al., 2001, A&A, 365, L7
Draine B. T., 2011, Physics of the Interstellar and Intergalactic Medium. Princeton Univ. Press, Princeton, NJ
Falgarone E., Verstraete L., Pineau Des Forêts G., Hily-Blant P., 2005, A&A, 433, 997
Galloway D. K., Muno M. P., Hartman J. M., Psaltis D., Chakrabarty D., 2008, ApJS, 179, 360
Gandhi P., Rao A., Johnson M. A. C., Paice J. A., Maccarone T. J., 2019, MNRAS, 485, 2642
García J. et al., 2009, ApJS, 185, 477
García J., Mendoza C., Bautista M. A., Gorczyca T. W., Kallman T. R., Palmeri P., 2005, ApJS, 158, 68
Gatuzz E. et al., 2013a, ApJ, 768, 60
Gatuzz E. et al., 2013b, ApJ, 778, 83
Gatuzz E., Churazov E., 2018, MNRAS, 474, 696
Gatuzz E., García J., Kallman T. R., Mendoza C., Gorczyca T. W., 2015, ApJ, 800, 29
Gatuzz E., Ness J.-U., Gorczyca T. W., Hasoglu M. F., Kallman T. R., García J. A., 2018a, MNRAS, 479, 2457
Gatuzz E., Rezaei K. S., Kallman T. R., Kreikenbohm A., Oertel M., Wilms J., García J. A., 2018b, MNRAS, 479, 3715
Gatuzz E., Gorczyca T. W., Hasoglu M. F., Schulz N. S., Corrales L., Mendoza C., 2020, MNRAS, 498, L20
Gomez S., Mason P. A., Robinson E. L., 2015, ApJ, 809, 9
Gorczyca T. W. et al., 2013, ApJ, 779, 78
Grimm H.-J., Gilfanov M., Sunyaev R., 2002, A&A, 391, 923
Gudennavar S. B., Bubbly S. G., Preethi K., Murthy J., 2012, ApJS, 199, 8
Gupta A., Mathur S., Krongold Y., 2017, ApJ, 836, 243
Hasoğlu M. F., Abdel-Naby S. A., Gatuzz E., García J., Kallman T. R., Mendoza C., Gorczyca T. W., 2014, ApJS, 214, 8
Hynes R. I., Steeghs D., Casares J., Charles P. A., O'Brien K., 2004, ApJ, 609, 317
in't Zand J. J. M., Kuulkers E., Verbunt F., Heise J., Cornelisse R., 2003, A&A, 411, L487
Jenkins E. B., Tripp T. M., 2011, ApJ, 734, 65
Jonker P. G., Nelemans G., 2004, MNRAS, 354, 355
Juett A. M., Schulz N. S., Chakrabarty D., 2004, ApJ, 612, 308
Juett A. M., Schulz N. S., Chakrabarty D., Gorczyca T. W., 2006, ApJ, 648, 1066
Kalberla P. M., Kerp J., 2009, ARA&A, 47, 27
Kallman T., Bautista M., 2001, ApJS, 133, 221
Knauth D. C., Meyer D. M., Lauroesch J. T., 2006, ApJ, 647, L115
Kuulkers E., den Hartog P. R., in't Zand J. J. M., Verbunt F. W. M., Harris W. E., Cocchi M., 2003, A&A, 399, 663
Liao J.-Y., Zhang S.-N., Yao Y., 2013, ApJ, 774, 116
Luo Y., Fang T., 2014, ApJ, 780, 170
McKee C. F., Ostriker J. P., 1977, ApJ, 218, 148
Meyer D. M., Cardelli J. A., Sofia U. J., 1997, ApJ, 490, L103
Miller M. J., Bregman J. N., 2013, ApJ, 770, 118
Miller M. J., Bregman J. N., 2015, ApJ, 800, 14
Moos H. W. et al., 2002, ApJS, 140, 3
Nandra K. et al., 2013, preprint (arXiv:1306.2307)
Ness J. U. et al., 2011, ApJ, 733, 70
Ness J.-U. et al., 2003, ApJ, 594, L127
Nicastro F., Senatore F., Gupta A., Guainazzi M., Mathur S., Krongold Y., Elvis M., Piro L., 2016a, MNRAS, 457, 676
Nicastro F., Senatore F., Krongold Y., Mathur S., Elvis M., 2016b, ApJ, 828, L12
Pinto C., Kaastra J. S., Costantini E., Verbunt F., 2010, A&A, 521, A79
Pinto C., Kaastra J. S., Costantini E., de Vries C., 2013, A&A, 551, A25
Piontek R. A., Ostriker E. C., 2007, ApJ, 663, 183
Ramírez J. M., Komossa S., Burwitz V., Mathur S., 2008, ApJ, 681, 965
Robin A. C., Reylé C., Derrière S., Picaud S., 2003, A&A, 409, 523
Smith R. K. et al., 2016, in den Herder J.-W. A., Takahashi T., Bautz M., eds, Proc. SPIE Conf. Ser. Vol. 9915, Space Telescopes and Instrumentation 2016: Ultraviolet to Gamma Ray. SPIE, Bellingham, p. 99054M
Smith R. A. N., Page M. J., Branduardi-Raymont G., 2007, A&A, 461, 135
Stanimirović S., Zweibel E. G., 2018, ARA&A, 56, 489
Steenbrugge K. C. et al., 2005b, A&A, 434, 569
Steenbrugge K. C., Kaastra J. S., Sako M., Brand uardi-Raymont G., Behar E., Paerels F. B. S., Blustin A. J., Kahn S. M., 2005a, A&A, 432, 453
Wang Z., Chakrabarty D., 2004, ApJ, 616, L139
Willingale R., Starling R. L. C., Beardmore A. P., Tanvir N. R., O'Brien P. T., 2013, MNRAS, 431, 394
Yao Y., Wang Q. D., 2006, ApJ, 641, 930

APPENDIX: SPECTRA OF INDIVIDUAL SOURCE AND BEST-FITTING MODELS

Figs A1 and A2 show the best-fitting models to the spectra for the individual LMXBs and extragalactic sources, respectively. For each source, all observations were combined for illustrative purposes. The black points correspond to the observations and the red lines indicate the best-fitting model. Residuals, in units of (*data* − *model*)/*error*, are included. The positions of the Kα and Kβ resonance lines are indicated for each ion, following the colour code used in Fig. 1.

Downloaded from https://academic.oup.com/mnras/article/504/3/4460/6256854 by NASA Goddard Space Flight Ctr user on 11 January 2022

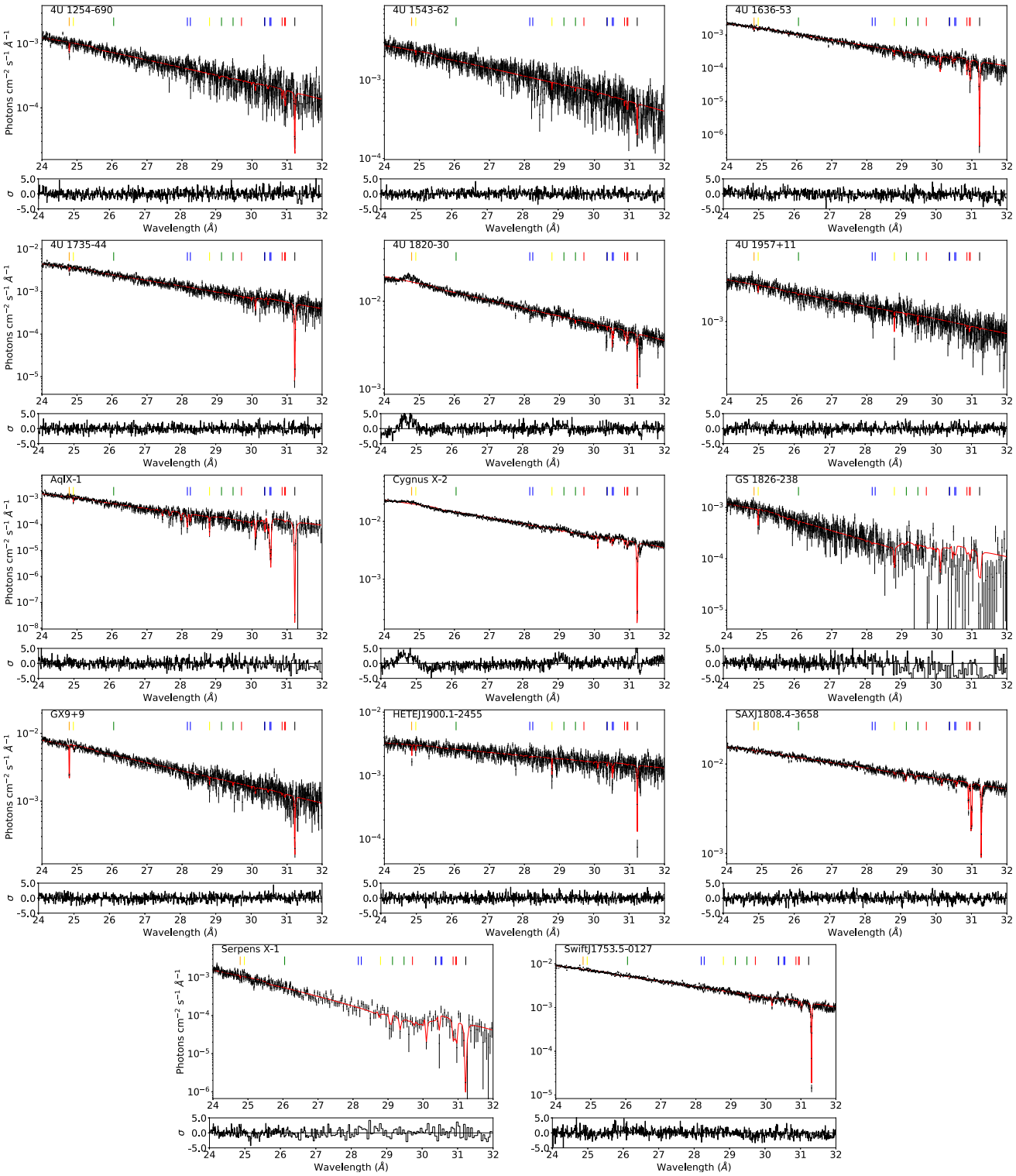


Figure A1. Best-fitting results in the N K-edge photoabsorption region for the LMXBs sample described in Table 1. In each panel, the black data points are the observations, while the solid red lines correspond to the best-fitting models.

Downloaded from https://academic.oup.com/mnras/article/504/3/4460/6256854 by NASA Goddard Space Flight Ctr user on 11 January 2022

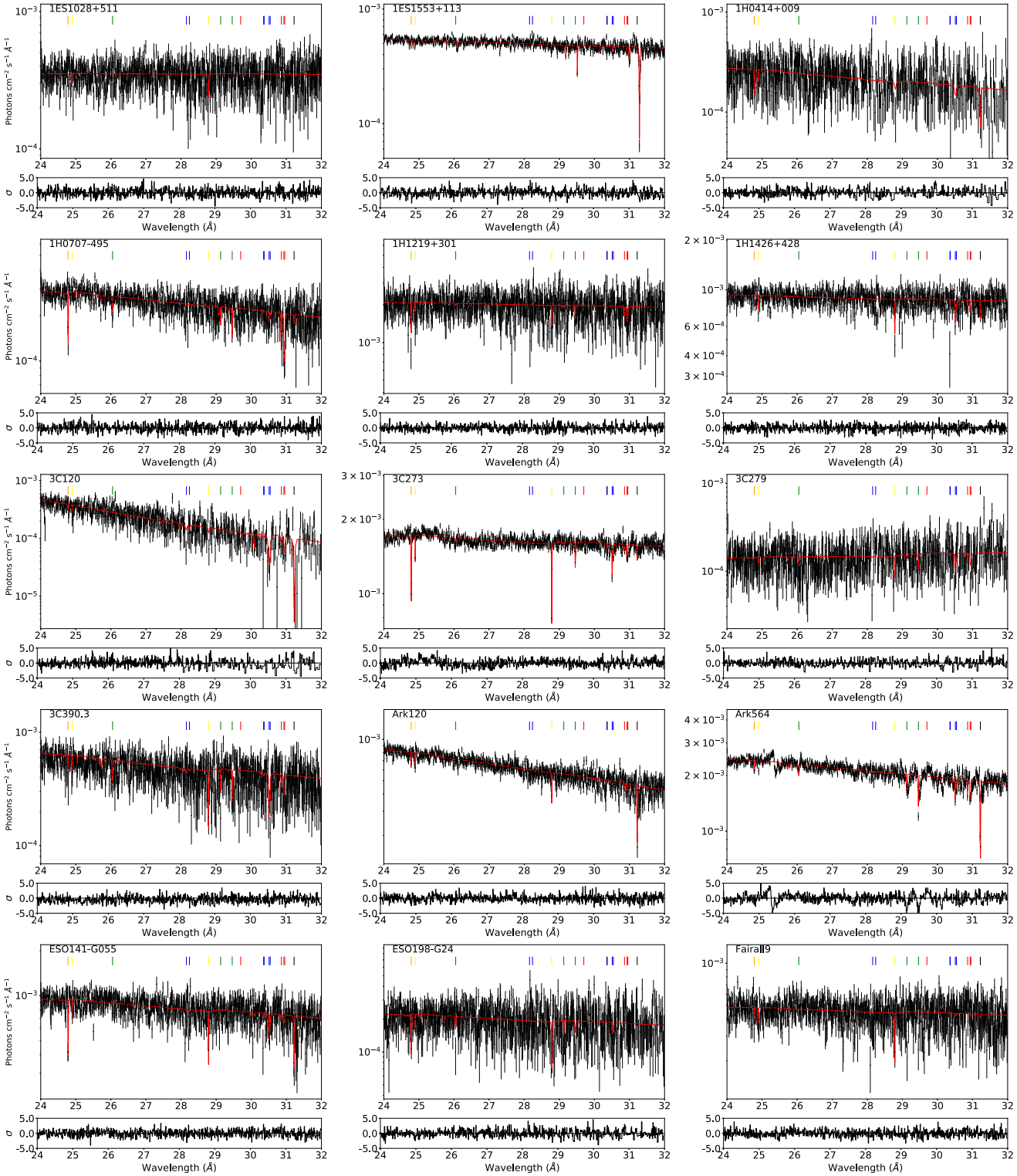


Figure A2. Best-fitting results in the N K-edge photoabsorption region for the Extragalactic sample described in Table 2. In each panel, the black data points are the observations and the solid red lines correspond to the best-fitting models.

Downloaded from https://academic.oup.com/mnras/article/504/3/4460/6256854 by NASA Goddard Space Flight Ctr user on 11 January 2022

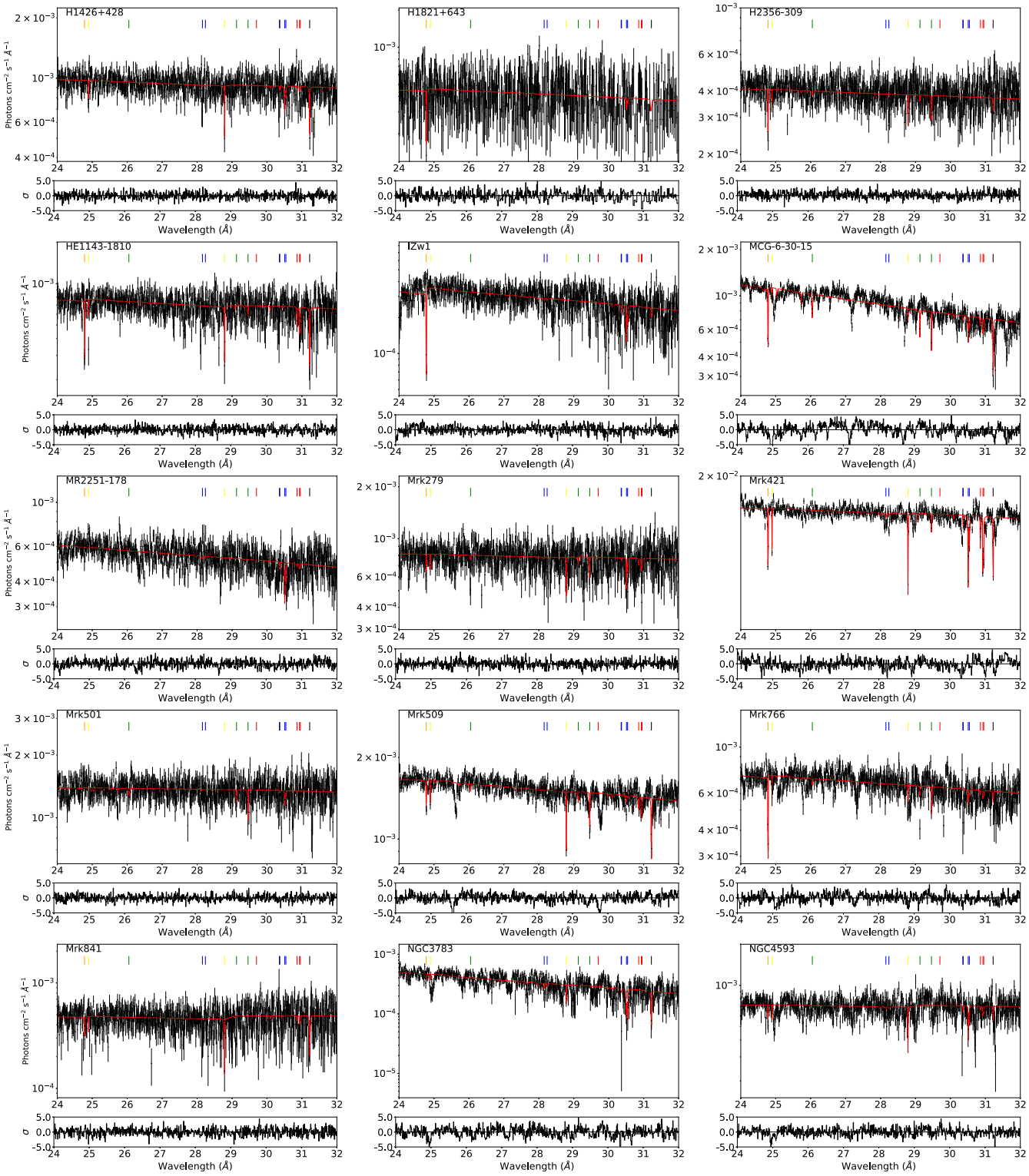


Figure A2. *continued*

Downloaded from https://academic.oup.com/mnras/article/504/3/4460/6256854 by NASA Goddard Space Flight Ctr user on 11 January 2022

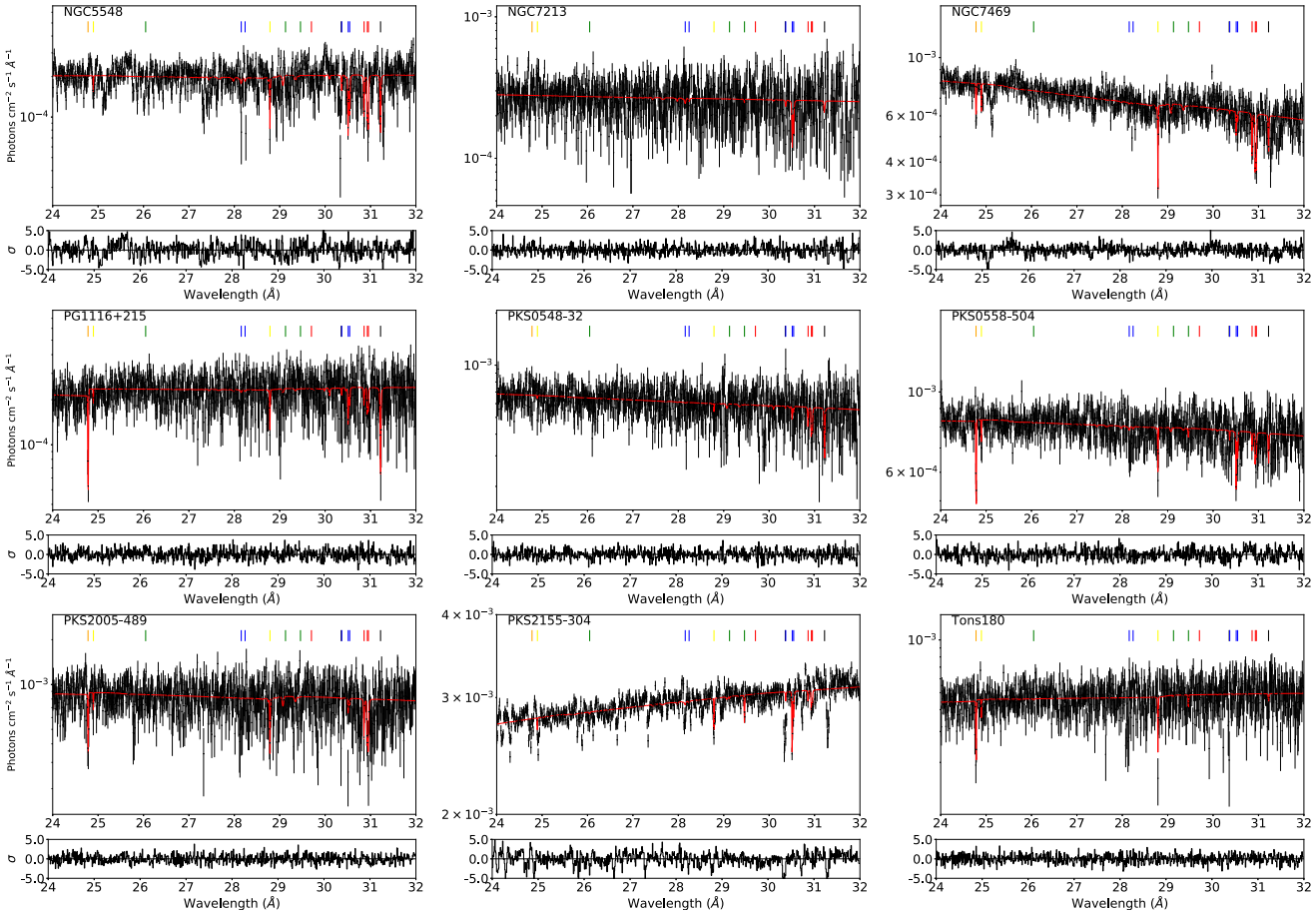


Figure A2. *continued*

This paper has been typeset from a TEX/LATEX file prepared by the author.

Downloaded from https://academic.oup.com/mnras/article/504/3/4460/6256854 by NASA Goddard Space Flight Ctr user on 11 January 2022